Chemical Science

Accepted Manuscript

This article can be cited before page numbers have been issued, to do this please use: P. Su, S. Lin and F. Xiao, *Chem. Sci.*, 2026, DOI: 10.1039/D6SC03862J.

ROYAL SOCIETY OF CHEMISTRY

rsc.li/chemical-science

Ligand-Amplified Quantum Tunneling in Polymer-Mediated Artificial Photosystems

View Article Online
DOI: 10.1039/D6SC03862J

Peng Su, Si-Han Lin, Fang-Xing Xiao *

College of Materials Science and Engineering, Fuzhou University, New Campus, Minhou, Fujian Province, 350108, China.

E-mail: fxxiao@fzu.edu.cn

Abstract

Quantum tunneling offers a fascinating paradigm for orchestrating spatial charge transport in artificial photosynthesis. However, precisely manipulating electron tunneling across well-defined heterointerfaces remains a formidable challenge, with conventional designs largely confined to classical Semiconductor-Insulator-Metal (S-I-M) architectures. Herein, we report a conceptual endeavor by fundamentally departing from the traditional S-I-M model, constructing a unique and novel Semiconductor-Insulator-Ligand/Metal tunneling platform. Specifically, an ultrathin insulating poly(sodium 4-styrenesulfonate) (PSS) layer is engineered onto a transition metal chalcogenide (TMC, e.g., CdS) substrate. Subsequently, poly(diallyldimethylammonium chloride) (PDDA)-capped metal nanocrystals (M@PDDA, M = Au, Pd) are precisely anchored via electrostatic self-assembly, yielding well-defined TMC@PSS/M@PDDA heterostructures. Distinct from conventional systems, the PDDA ligands synergistically couple with the metal core to form an integrated, highly potent electron capture center driven by the Schottky-junction effect. This unique synergistic driving force triggers non-classical, directional electron tunneling from the photoexcited TMC substrate directly through the insulating PSS barrier. Benefiting from this advantageous Quantum tunneling, TMC@PSS/M@PDDA heterostructures demonstrate significantly enhanced and multifarious visible-light-driven photoredox activities including selective organic transformations and H_2O_2 production.

This work establishes an elegant conceptual paradigm for decoding and customizing quantum tunneling pathways, offering profound fundamental insights into advanced solar energy conversion.

View Article Online
DOI: 10.1039/D6SC03862J

Keywords: Quantum tunneling, Self-assembly, Charge transport, Non-conjugated polymers, Metal nanocrystals.

1. Introduction

Solar-driven artificial photosynthesis represents a highly compelling paradigm for sustainable solar-to-chemical energy conversion.[1-3] In recent years, diverse semiconductor-based platforms have been extensively explored, among which transition metal chalcogenides (TMCs) have garnered widespread attention owing to their substantial light absorption coefficients, abundant catalytic active sites, and highly tunable electronic band structures.[4-6] Nevertheless, the practical realization of highly efficient TMC-based photosystems is fundamentally impeded by severe exciton recombination, sluggish interfacial charge-transfer kinetics, and inherent susceptibility to photocorrosion. Overcoming these thermodynamic and kinetic hurdles necessitates the precise orchestration of interfacial charge transport pathways.[7, 8]

Quantum tunneling of photogenerated charge carriers has emerged as a fascinating strategy to radically accelerate charge-transfer kinetics by bypassing classical thermodynamic interfacial energy barriers. Conventional charge-tunneling photosystems, however, are predominantly confined to classic Semiconductor-Insulator-Metal (S-I-M) architectures, typically employing rigid inorganic insulating layers (e.g., Al_2O_3, SiO_2) as the interfacial barrier. In such classical scenarios, electrons directionally tunnel through the ultrathin insulating medium and are subsequently extracted by the outermost metal co-catalysts, driven by the Schottky-junction effect. While this spatial decoupling effectively prolongs carrier lifetimes and promotes catalytic activity, these rigid inorganic insulating layers suffer from inherently poor interfacial adaptability. They struggle to maintain structural integrity and efficient synergistic activity within complex, dynamic

photoredox environments. Consequently, unlocking the full potential of quantum tunneling in versatile, liquid-phase artificial photosynthetic systems remains a formidable challenge.

View Article Online
DOI: 10.1039/D6SC03862J

Inspired by the intrinsic dielectric nature of non-conjugated polymers (NCPs), we envision that the classical S-I-M paradigm can be fundamentally reinvented by substituting rigid inorganic barriers with flexible NCPs.[9-16] Beyond serving as robust electron-tunneling barriers, NCPs feature exceptional structural conformability and interfacial processability. This unique flexibility facilitates the conformal integration of ultrathin polymer layers and metal nanocrystals (NCs) onto TMC substrates. Concurrently, while surface ligands are indispensable for stabilizing monodisperse colloidal metal NCs, their characteristic electrostatic properties render them highly programmable building blocks for directed self-assembly. Therefore, we propose that the rational integration of polymer-encapsulated TMCs with ligand-capped metal NCs (metal@ligand) via electrostatic interactions enables the construction of structurally novel, polymer-mediated quantum tunneling photosystems. Notably, conventional wisdom dictates that insulating capping ligands inevitably passivate and sterically shield the catalytic active sites of metal NCs. Consequently, exploring the active electronic cooperation between peripheral ligands and the metal core to intentionally amplify the interfacial Schottky-junction effect represents a largely uncharted, yet profoundly promising, frontier in quantum tunneling catalysis.[17-20]

Herein, we conceptually demonstrate the rational design of a unique Semiconductor-Insulator-Ligand/Metal tunneling platform. Specifically, through highly controllable electrostatic self-assembly, tailored M@PDDA (M = Au, Pd) NCs were precisely loaded onto CdS substrates pre-coated with an ultrathin poly(sodium 4-styrenesulfonate) (PSS) insulating layer, constructing well-defined CdS@PSS/M@PDDA (C@P/M) heterostructures. Crucially, consistent with our proposed hypothesis, M@PDDA NCs are not merely a passive electron acceptor, but rather, through the synergistic electronic coupling between PDDA ligands and the metal core, significantly enhance the interfacial Schottky junction effect and thereby transform

into an efficient electron capture center. This customized interfacial driving force triggers non-classical, unidirectional electron tunneling from the photoexcited CdS substrate through the insulating PSS barrier to the terminal M@PDDA NCs. Additionally, using photoredox reactions such as selective reduction of aromatic nitro compounds and hydrogen peroxide generation as probes, we confirmed the effectiveness of this interfacial tunneling kinetics under visible light conditions. Ultimately, this work unveils the emerging potential of NCP in customizing a new generation of quantum tunneling artificial photosystems for advanced solar energy conversion.

2. Experimental section

2.1 Materials

Cadmium acetate dihydrate ($C_4H_6CdO_4·2H_2O$), Thiourea (CH_4N_2S), Hydrofluoric acid (HF 40 wt%), Poly(sodium 4-styrenesulfonate) solution (PSS) (M_w=70000, 30 wt% in H_2O) , sodium chloride (NaCl), Sodium hydroxide (NaOH), Poly(diallyldimethylammonium chloride) solution (PDDA) (M_w=200000~350000, 20 wt% in H_2O), gold (III) chloride trihydrate ($HAuCl_4·3H_2O$, 99.9%), 4-nitroaniline (4-NA), 3-nitroaniline (3-NA), 2-nitroaniline (2-NA), 2-nitrophenol (2-NP), Nitrobenzene, 2-nitroacetophenone, Ammonium formate (NH_4HCO_2), and deionized water (DI H_2O, Millipore, 18.2 MΩ cm resistivity) are used.

2.2 Preparation of catalysts

2.2.1 Preparation of CdS nano-leaves

$C_4H_6CdO_4·2H_2O$ (5 mmol), CH_4N_2S (6 mmol), HF (40 wt%, 0.805 mL) and DI H_2O (79.2 mL) were added into a 100 mL Teflon autoclave to 80% volume. After stirring at room temperature for 1.5 h, the autoclave was sealed and maintained at 200 ˚C for 20 h, and then air cooled to room temperature. The

precipitate obtained was filtered and washed several times with DI H_2O and absolute ethanol, and then dried in vacuum at 60 ˚C for 8 h.[3]

View Article Online
DOI: 10.1039/D6SC03862J

2.2.2 Preparation of Au@PDDA nanocrystals (Au@PDDA NCs)

400 μL PDDA (20% in water), 80 mL DI H_2O, 200 μL 0.5 M NaOH and 200 μL $HAuCl_4$ (40 mg mL^{-1}) were added into a beaker. After thoroughly mixing for 2 mins, the mixed solution was maintained at 100 ˚C for 4 h. Through accurately controlling the reaction time and using an inverted culture dish to cover the beaker to avoid the rapid vaporization of the reaction liquid, the Au@PDDA NCs were thus obtained.[7]

2.2.3 Preparation of Pd@PDDA nanocrystals (Pd@PDDA NCs)

Briefly, 400 μL PDDA (20% in water), 80 mL DI H_2O, 200 μL 0.5 M NaOH and 300 μL Na_2PdCl_4 (20 mg mL^{-1}) were added into a beaker. After thoroughly mixing for 5 mins, the mixed solution was maintained at 100 ˚C for 26 h.[7]

2.2.4 Preparation of CdS@PSS (C@P)

0.2 g CdS nano-leaves were directly added into 40 mL PSS aqueous solution (0.5 mg mL^{-1}, 0.5 M NaCl, pH=10). The mixture was stirred for 1 h and centrifuged, and then dried in vacuum at 60 ˚C for 10 h.[21]

2.2.5 Preparation of CdS@PSS/Au@PDDA (C@P/Au) heterostructures

The construction of C@P/Au heterostructures were obtained by electrostatic self-assembly using CdS@PSS as the substrate and Au@PDDA NCs as the anchoring block. Specifically, Au@PDDA NCs aqueous solution was added dropwise into 50 mg of CdS@PSS aqueous dispersion according to the mass ratio under vigorous stirring. After mixing for 2 h, the mixtures were centrifuged and labeled as C@P/Au-X (X = 0.1, 0.25, 1, 4, 7, wt%), and then dried in vacuum at 60 ˚C for 8 h.

2.2.6 Preparation of CdS@PSS/Pd@PDDA (C@P/Pd)

C@P/Pd counterpart was fabricated using the identical synthetic procedures to that of C@P/Au, except that the Au@PDDA NCs were replaced with Pd@PDDA NCs.

View Article Online
DOI: 10.1039/D6SC03862J

2.3 Characterization

X-ray diffraction (XRD, Miniflex600) is utilized to determine the crystal structure. Fourier transform infrared (FTIR) spectra are monitored on an infrared spectrophotometer (TJ270-30A). UV-visible diffuse reflectance spectra (DRS) are tested on Cary50 (Varian, America). X-ray photoelectron spectra (XPS, Thermal Fisher) are measured with binding energy corrected by 284.80 eV. Field-emission Scanning electron microscopy (FESEM, Carl Zeiss) and Transmission electron microscopy (TEM, Tecnai G2 F20) are harnessed to explore the morphologies. Solid photoluminescence (PL) spectra are measured on an Eclipse spectrometer. Zeta potential (ξ) measurements were performed by dynamic light scattering analysis (Zeta sizer Nano ZS-90). Time-resolved photoluminescence (TRPL) spectra were recorded on a FLS 920 fluorescence lifetime spectrophotometer (Edinburgh, Instruments, UK). Brunauer-Emmett-Teller (BET) specific surface area and N_2 adsorption experiments are carried out on a 2460.

2.4 Photocatalytic performances

2.4.1 Aromatic nitro compounds reduction

A mixture containing 10 mg of catalyst and 40 mg of NH_4HCO_2 (as hole scavenger) was dispersed in 30 mL of 4-NA aqueous solution (20 ppm) within a glass reactor under N_2 bubbling. After vigorous stirring in the dark for 15 mins to establish the adsorption-desorption equilibrium, the system was irradiated with visible light ($\lambda > 420$ nm). Aliquots (2 mL) were collected at specified time intervals (0, 15, 30, 45, 60, 75 s), centrifuged at 12,000 rpm, and the supernatant was analyzed by UV-vis spectrophotometry. Photoreduction of other nitroaromatic compounds (3-NA, 2-NA, NP, Nitrobenzene and 2-Nitroacetophenone) were performed under the identical conditions. Photocatalytic activities of the samples were quantified using the following

equation:

View Article Online
DOI: 10.1039/D6SC03862J

$$\text{Conversion (\%)} = \frac{C_0 - C_{\text{Nitrobenzene}}}{C_0} \times 100\% \quad \textbf{(Equation 1)}$$

2.4.2 H_2O_2 production

Using a syringe equipped with a filter head, 3 mL of the reaction mixture (maintained under oxygen atmosphere) was extracted, and the H_2O_2 production rate was quantified by UV-Vis spectrophotometry (Thermo Genesis). Specifically, a homogeneous mixture was prepared by combining 45 mL of DI H_2O with 5 mL of methanol. 35 mg of catalyst was added to the solution and dispersed via magnetic stirring for 5 mins. The reactor was purged with O_2 for 15 mins in the dark. Photocatalytic reactions were conducted under a 300 W Xe lamp equipped with a cutoff filter ($\lambda > 420$ nm) with continuous stirring and a cooling circulator to maintain the constant temperature. Aliquots (1 mL) were collected at specified intervals (0, 5, 15, 20, 25 min). For H_2O_2 quantification, 1 mL of the reaction sample， 50 μL of N, N-diethyl-p-phenylenediamine sulfate (DPD), and 50 μL of catalase (source horseradish) (POD) solution was added to a 10 mL centrifuge tube. The mixture was then diluted to 10 mL with DI H_2O. From this solution, a 3 mL aliquot was taken for absorbance measurement at 551 nm using UV-Vis spectrophotometry. The H_2O_2 concentration was determined by referencing the standard calibration curve (**Figure S21**).

Apparent quantum yield (A.Q.Y) of the reaction was defined by the following equations:[22, 23]

$$\text{A.Q.Y} = \frac{2 \times number\ of\ evolved\ H_2O_2\ molecules}{M} \times 100\% \quad \textbf{(Equation 2)}$$

$$M = \frac{\lambda E}{hc} \quad \textbf{(Equation 3)}$$

In the equation, E, λ, h and c are the average intensity of irradiation, the wavelength of the irradiation, Planck constant and the speed of light, respectively. A.Q.Y value were measured under the same photocatalytic reaction conditions except for using the monochromatic light with different wavelength (i.e., 420, 450, 500, 520, 550 nm) as the light source. The number of incident photons was measured using a radiant

power energy meter (Perfect light, PLS-MW2000).

View Article Online
DOI: 10.1039/D6SC03862J

2.5 Photoelectrochemical (PEC) measurements

PEC measurements were performed using an electrochemical workstation (CHI660E, CH Instruments, Shanghai) equipped with a conventional three-electrode system comprising a Pt foil counter electrode (1 cm × 1 cm), an Ag/AgCl reference electrode (saturated KCl), and a working electrode. A 0.5 M Na_2SO_4 aqueous solution (pH=6.69) served as the electrolyte. The working electrode was fabricated on fluorine-doped tin oxide (FTO) glass through the following procedure: First, the FTO substrate was masked with Scotch tape to define an active area of 1 cm^2. Subsequently, 15 mg of the sample was ultrasonically dispersed in 3 mL of ethanol to form a homogeneous slurry, which was then uniformly coated onto the pretreated FTO surface. Following air-drying, the tape was carefully removed, and the non-active areas were insulated with nail polish. For measurements, the prepared working electrode was vertically immersed in the electrolyte and illuminated under visible light ($\lambda > 420$ nm) using a 300 W Xenon lamp (PLS-ske300d, Beijing Perfect light Co. Ltd, China). The electrode potentials were calibrated versus the reversible hydrogen electrode (RHE) using the following equation:[24]

$$E_{RHE} = E_{Ag/AgCl} + 0.059\ pH + E^{\circ}_{Ag/AgCl}\ (E^{\circ}_{Ag/AgCl} = 0.1976\ V\ at\ 25\ ^{\circ}C) \quad (\textbf{Equation 4})$$

3. Results and discussion

3.1 Structural characterizations

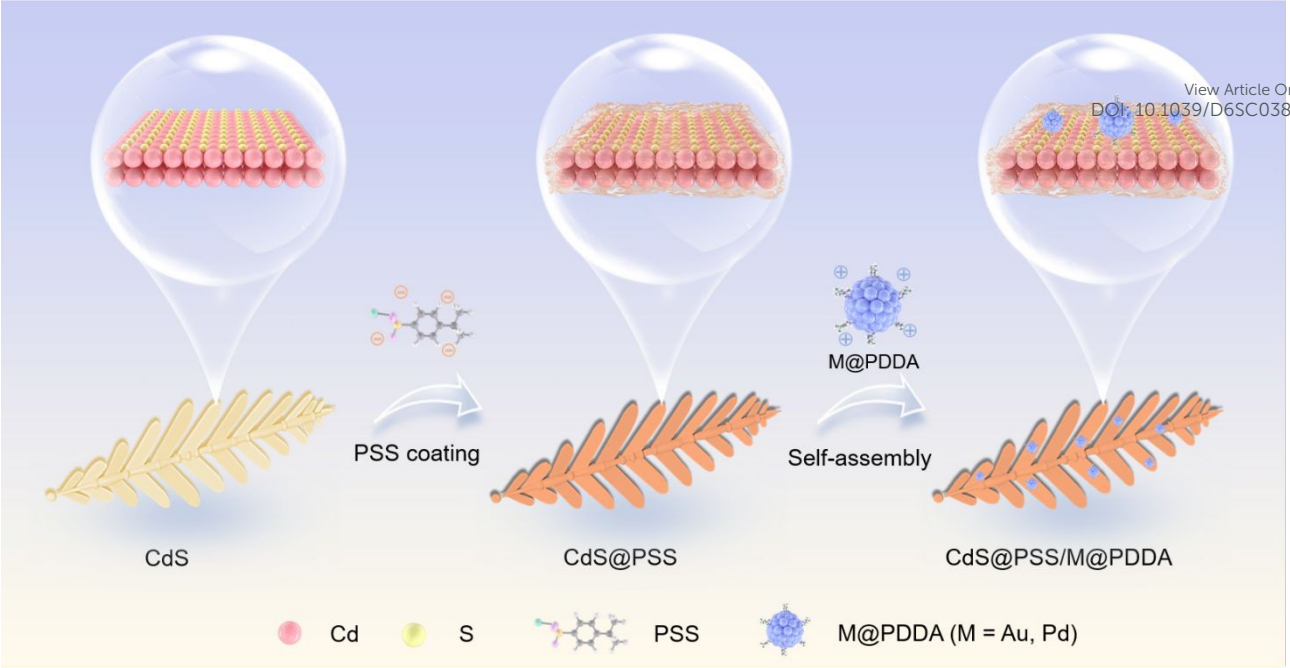

Scheme 1. Schematic flowchart for self-assembly of C@P/M (M= Au, Pd) heterostructures.

The detailed fabrication of the C@P/Au heterostructure is illustrated in **Scheme 1**. Initially, CdS substrate was functionalized with an ultrathin layer of poly(sodium 4-styrenesulfonate) (PSS) (**Figure S1**), imparting a negatively charged surface. Concurrently, tailor-made Au NCs coated with a polymer ligands of poly(diallyldimethylammonium chloride) (PDDA) (**Figure S2**) demonstrate a positively charged surface. Under ambient conditions, oppositely charged CdS@PSS and Au@PDDA NCs undergo electrostatic self-assembly leading to the C@P/Au heterostructure. The feasibility of this ligand-induced electrostatic self-assembly was verified by the zeta potential analysis (**Figure S3**). C@P/Pd heterostructure was also fabricated using the analogous synthetic approach.

The morphologies and microstructures of the samples were characterized by field-emission scanning electron microscopy (FESEM) and transmission electron microscopy (TEM). As shown in **Figures 1a & d**, pristine CdS displayed a leaf-like structure with dimension in the range of 3-8 μm. This unique nano-leaf structure is beneficial for exposing a high density of active sites and shortening the vertical migration distance of charge carriers, thereby effectively suppressing the charge recombination.[31] When the CdS surface was

wrapped with PSS (C@P), no obvious morphology alteration is observed relative to pure CdS (**Figures 1b & e**). This is primarily attributed to the extremely low electron contrast of the ultrathin PSS layer, which makes it difficult to generate sufficient visual differentiation in conventional SEM and low-magnified TEM images, thereby rendering it challenging to directly distinguish from other components. SEM and TEM images of C@P/Au-0.25 (**Figures 1c & f**) revealed the sporatic attachment of Au@PDDA NCs on the CdS nano-leaf surfaces, indicating that Au@PDDA NCs have been successfully anchored onto the C@P surface via electrostatic self-assembly. The characterizations of the Au@PDDA NCs were demonstrated in **Figure S4a**. The average diameter of Au@PDDA NCs was approximately 14 nm (**Figures S4b & c**). High-resolution transmission electron microscopy (HRTEM) images further validate the above speculation. As shown in **Figure 1g**, pristine CdS exhibited a well-defined crystalline structure with lattice fringe of approximately 0.336 nm, corresponding to the (200) crystal plane of hexagonal CdS.

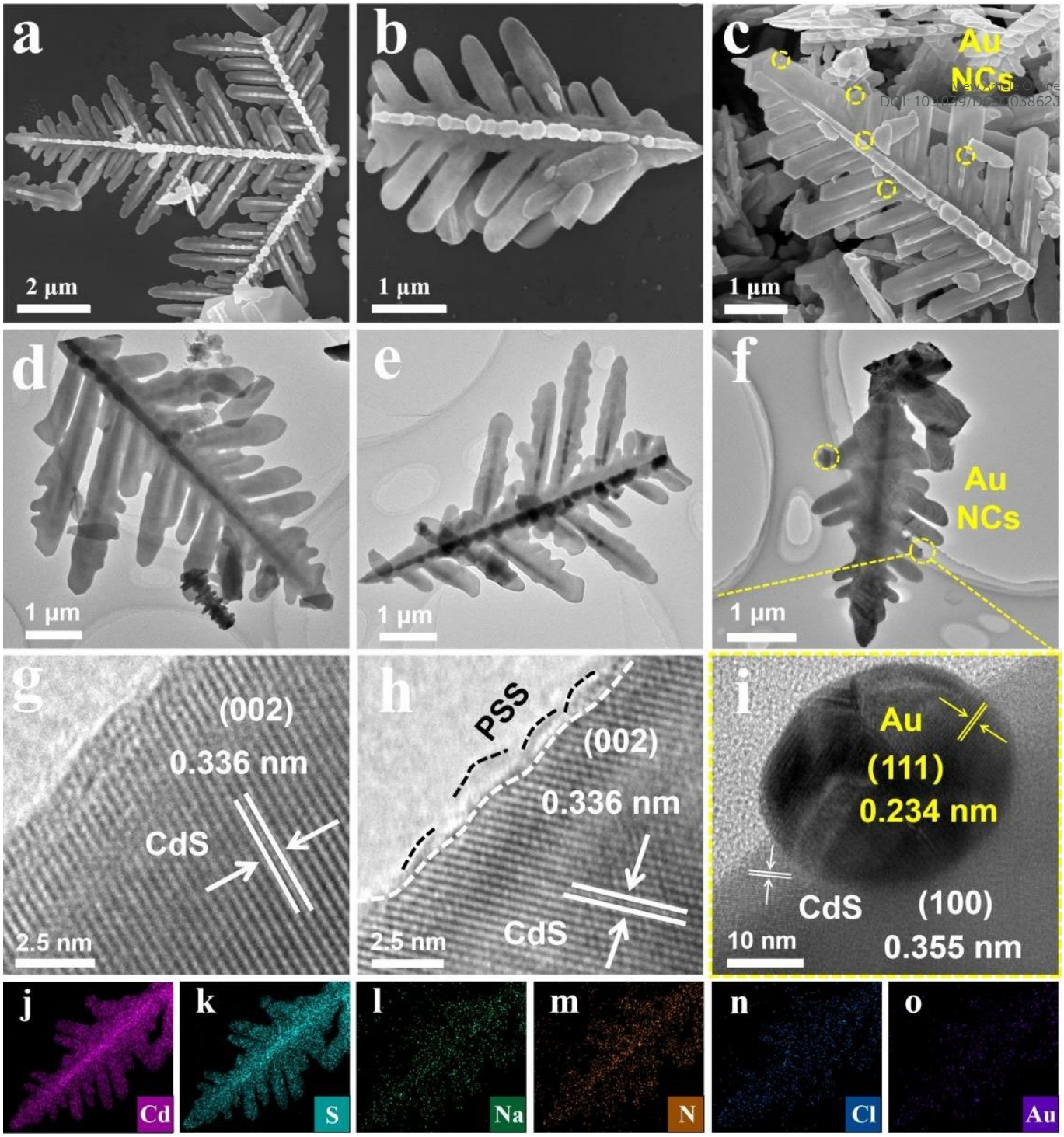

Figure 1. (a-c) SEM images of CdS, C@P and C@P/Au-0.25, low-magnified TEM images of (d-f) CdS, C@P and C@P/Au-0.25, HRTEM images of (g) CdS, (h) C@P, (i) C@P/Au-0.25, and elemental mapping results of (j-o) C@P/Au-0.25.

In the HRTEM image of C@P (**Figure 1h**), besides the distinguishable lattice fringe of CdS (0.336 nm), an amorphous PSS thin layer was found to be tightly wrapped around the outer surface of CdS, as indicated by the black dashed line. **Figure 1i** clearly demonstrated the intimate integration between C@P and Au@PDDA, where the lattice fringes of 0.234 nm and 0.355 nm correspond to the (111) and (100) crystal

planes of cubic Au nanocrystals and hexagonal CdS, respectively. These results confirm the successful enwrapping of CdS by PSS and anchoring of Au@PDDA onto the C@P surface. Furthermore, TEM elemental mapping (**Figures 1j-o**) provided more intuitive evidence for the successful preparation of the target sample. The coexistence of Cd, S, Na, N, Cl, and Au elements in C@P@Au-0.25, with their signals distributed along the nanoleaf framework, implies that PSS and Au@PDDA have been successfully integrated on the CdS substrate. This conclusion was also supported by the EDS results (**Figure S5**).

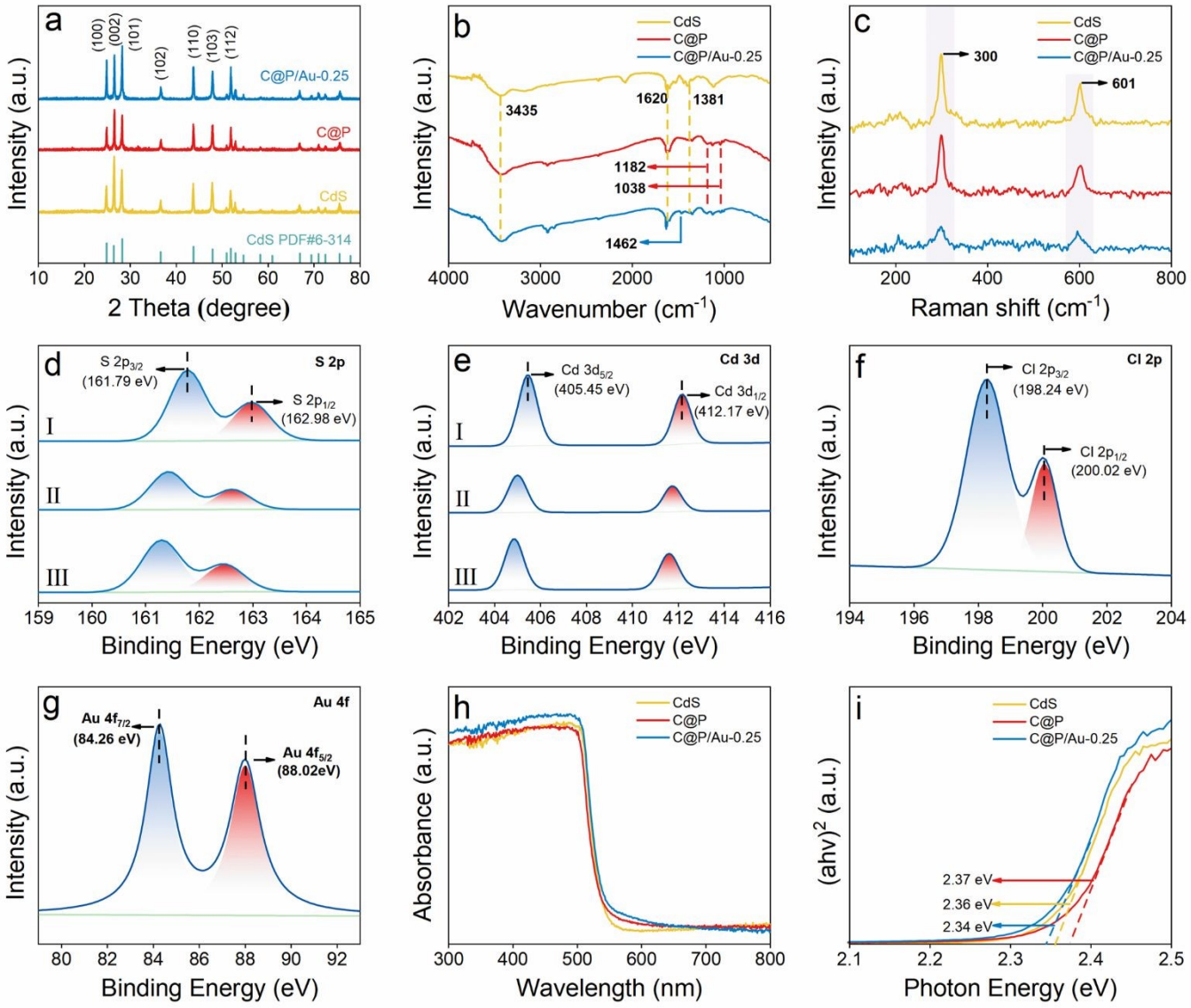

Figure 2. (a) XRD patterns, (b) FTIR and (c) Raman spectra of CdS, C@P and C@P/Au-0.25. High-resolution (d) S 2p and (e) Cd 3d spectra of (I) CdS, (II) C@P and (Ⅲ) C@P/Au-0.25. High-resolution (f) Cl 2p and (g) Au 4f spectra of C@P/Au-0.25. (h) DRS results of CdS, C@P, and C@P/Au-0.25 with (i) transformed plots based on the Kubelka-Munk function vs. energy of light.

X-ray diffraction (XRD) analysis was employed to investigate the crystal structures of CdS, C@P, and C@P/Au-0.25. As illustrated in **Figure 2a**, all the samples exhibit characteristic diffraction peaks at 24.90°, 26.56°, 28.23°, 36.68°, 43.78°, 47.84°, and 51.83°, which are indexed to the (100), (002), (101), (102), (110), (103), and (112) crystal planes of hexagonal CdS (PDF#6-314), respectively.[25] The result suggests that neither PSS modification nor Au@PDDA loading alters the crystalline phase of CdS substrate. However, the characteristic diffraction peaks of Au@PDDA NCs are also not detected in the XRD pattern of C@P/Au-0.25, which could be attributed to the relatively low loading content of Au@PDDA NCs. The Fourier transform infrared (FTIR) spectra of the samples were shown in **Figure 2b**, with the corresponding functional group assignments summarized in **Table S1**. Notably, the characteristic vibrational bands at 1182 cm^{-1} and 1038 cm^{-1} observed for both C@P and C@P/Au-0.25 are assigned to the $-SO_3$ groups from PSS, confirming the encapsulation of PSS on the CdS surface.[26] Furthermore, the band at 1462 cm^{-1} in the FTIR spectrum of C@P@Au-0.25 corresponds to the bending vibration mode of $-CH_2$ functional groups from PDDA, providing clear evidence for the anchoring of Au@PDDA NCs on the CdS substrate.[27] **Figure 2c** showed the decreased Raman intensity in C@P and C@P/Au-0.25 versus pristine CdS, verifying the PSS encapsulation and Au@PDDA anchoring and thus shielding the peaks. X-ray photoelectron spectroscopy (XPS) measurements were conducted to elucidate the elemental chemical states of the samples and unravel the synergistic effect among CdS, PSS, and Au@PDDA. Survey spectrum of C@P/Au-0.25 (**Figure S6a**) exhibits the characteristic signals of Cd, S, Au, N, and Cl, among which Au originate from Au@PDDA NCs and N & Cl are from PDDA ligands. In the high-resolution Cl 2p spectrum of C@P/Au-0.25, the peaks at 198.24 eV (Cl $2p_{3/2}$) and 200.02 eV (Cl $2p_{1/2}$) (**Figure 2f**) are assigned to the Cl^- species from PDDA. The presence of Au 4f doublet at 84.26 eV (Au $4f_{7/2}$) and 88.02 eV (Au $4f_{5/2}$) (**Figure 2g**) confirms the metallic Au(0) state, indicating the successful synthesis and loading of Au@PDDA NCs.[28] Moreover, high-resolution Na 1s spectrum of C@P/Au-0.25 demonstrates the peak at 1072.12 eV which stems from PSS (**Figure S6c**), verifying its encapsulation on the

CdS substrate, consistent with the FTIR and Raman results. Significantly, binding energy shifts are observed for both Cd and S in C@P and C@P/Au-0.25 compared with pristine CdS (**Figure 2d & e**), revealing electronic interaction between CdS, PSS, and Au@PDDA NCs. In summary, the XPS results compellingly confirm that Au@PDDA NCs and PSS can be stably loaded onto the CdS substrate through ligand-induced electrostatic self-assembly.

The light absorption capacity of the samples was explored by UV-visible diffuse reflectance spectroscopy (DRS). As shown in **Figure 2h**, all the samples exhibit a characteristic absorption band edge at 500 nm, which originated from the intrinsic bandgap photoexcitation of the CdS substrate. Compared with CdS and C@P, C@P/Au-0.25 demonstrated enhanced light absorption in the visible region (500-700 nm). Combined with **Figure S4a**, this is primarily attributed to the dominant contribution from the intrinsic absorption of Au@PDDA NCs within this wavelength region. It is noteworthy that although Au@PDDA NCs typically exhibit a surface plasmon resonance (SPR) effect, no obvious SPR peak was observed in the DRS results of C@P/Au-0.25, which was caused by the excessively low loading content of Au@PDDA NCs.[29] The band gaps (E_g) of the samples were calculated using the Kubelka-Munk function below (**Equation 5**):[30]

$$(\alpha h\nu)^2 = A\,(h\nu - E_g) \qquad \textbf{(Equation 5)}$$

where α, hν, and A represent the absorption coefficient, photon energy, and constant, respectively. The E_g values of CdS, C@P, and C@P/Au-0.25 were determined to be 2.36, 2.37, and 2.34 eV (**Figure 2i**), respectively, indicating that neither the PSS coating nor Au@PDDA NCs deposition substantially alter the E_g value of the CdS substrate. Nevertheless, the loading of Au@PDDA NCs still significantly enhances the light absorption efficiency of the composite material in the visible light region. N_2 adsorption-desorption measurements reveal that CdS, C@P, and C@P/Au-0.25 all exhibit typical Type IV isotherms (**Table S3**). Specifically, with the introduction of PDDA and Au@PDDA NCs, the specific surface area progressively increases from 3.803 m^2/g (CdS) to 3.952 m^2/g (C@P) and further to 4.871 m^2/g (C@P/Au-0.25). Evidently,

the successful loading of PDDA and Au@PDDA NCs effectively enhances the specific surface area of the CdS substrate, which is conducive to providing more active sites for participating in photocatalytic reactions.

3.2 Photocatalytic activities

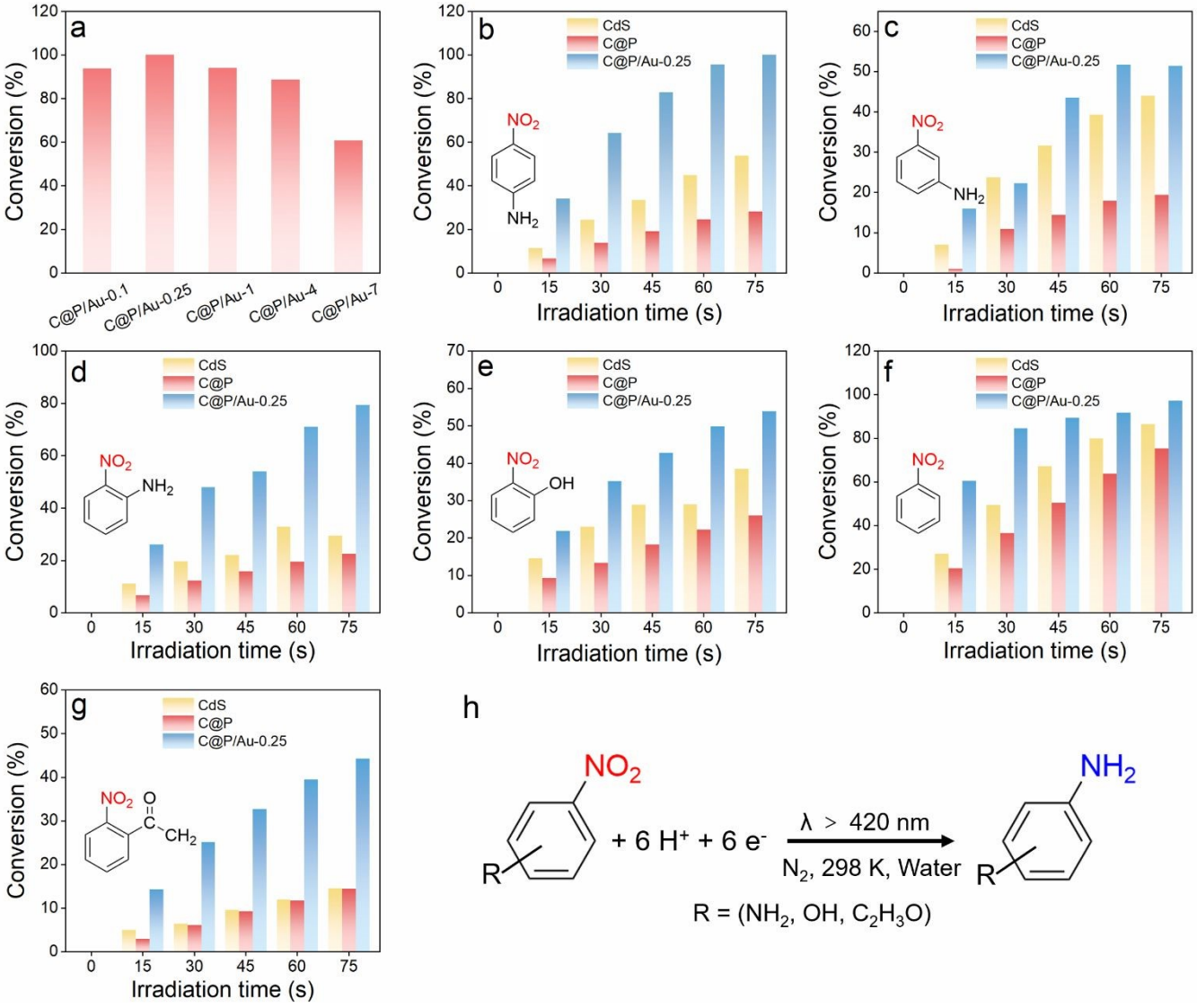

Figure 3. (a) Photocatalytic selective reduction of 4-NA over C@P/Au-X (X: 0.1, 0.25, 1, 4, 7) with different mass ratios of Au@PDDA NCs under visible light (λ > 420 nm) irradiation with the addition of ammonium formate as hole scavenger and N_2 bubbling under ambient conditions, and photocatalytic performances of CdS, C@P and C@P/Au-0.25 toward selective reduction of nitroaromatics under the same conditions including (b) 4-NA, (c) 3-NA, (d) 2-NA, (e) 2-NP, (f) nitrobenzene and (g) 2-Nitroacetophenone. (h) Typical reaction model under the current experimental conditions.

Using ammonium formate as the hole scavenger, photocatalytic performances of the samples for the conversion of aromatic nitro compounds to amino derivatives were investigated under visible light irradiation (λ > 420 nm). As illustrated in **Figure 3a**, to clarify the effect of Au@PDDA NCs loading content on the

photocatalytic performance of the C@P/Au heterostructure and screen out the optimal sample, a gradient optimization of the Au@PDDA NCs loading ratio was systematically conducted. The results suggest that the conversion efficiency of 4-nitroaniline (4-NA) by the C@P/Au heterostructure exhibits a distinct "volcano-type" variation trend with increasing Au@PDDA NCs loading, and the optimal photoactivity is achieved when the loading ratio of Au@PDDA NCs was set at 0.25%. As depicted in **Figure 3b**, constrained by intrinsic photocorrosion and sluggish charge transfer, pristine CdS exhibited a mere 49% reduction efficiency for 4-NA under visible light irradiation. When the surface of CdS was wrapped with an ultrathin PSS layer to form the C@P, its photocatalytic activity are markedly decreased. This is attributed to the fact that PSS, as a non-conjugated insulating polymer, hinders the interfacial charge transport process, making it difficult for photogenerated charge carriers to reach the surface and participate in catalytic reactions. Notably, after anchoring Au@PDDA NCs on the surface of C@P via electrostatic self-assembly, photocatalytic performance of C@P/Au-0.25 towards 4-NA reduction was remarkably enhanced, with a total conversion rate reaching nearly 100% under the same conditions. The remarkable performance disparity between C@P and C@P/Au-0.25 compellingly corroborates the pivotal role of Au@PDDA NCs in capturing photogenerated electrons and surmounting the transport barrier imposed by the PSS insulating layer. In other words, we speculate that within the C@P/Au-0.25 heterostructure, electrons photoexcited over CdS traverse the PSS layer with the help of Au@PDDA NCs which function as high-performance electron-withdrawing pump, thus ultimately enabling the efficient photocatalytic reduction of aromatic nitro compounds at the Au@PDDA NCs sites.

To verify that the aforementioned process is a photocatalytic process, control experiments were further performed. The results reveal that the conversion rate of 4-NA remains negligible without light or catalyst (**Figure S8a & b**), implying it is indeed a photocatalytic reaction. This conclusion is also confirmed in the H_2O_2 generation reaction. From a kinetic perspective, efficient carrier separation and directed carrier migration capability are the core prerequisites for achieving high photocatalytic conversion rate of aromatic nitro

compounds. To gain deeper insights into the decisive role of electrons in triggering the photoreduction performance of C@P/Au-0.25, electron trapping experiments were conducted. In the presence of $AgNO_3$ as an electron scavenger, photocatalytic activity of C@P/Au-0.25 was almost negligible (**Figure S9a**). Evidently, electrons serve as the active species that drives the photoreduction reaction. Under the same conditions, photocatalytic reduction of other aromatic nitro compounds such as 2-nitroaniline (2-NA), 3-nitroaniline (3-NA), nitrophenol (NP), nitrobenzene and 2-nitrophenol (2-NP) over the same catalysts were also performed. The results consistently demonstrated that the C@P/Au-0.25 ternary heterostructure maintains the optimal photocatalytic activity, strongly revealing that the tunneling effect induced by Au@PDDA NCs can effectively overcome the PSS barrier layer, exhibiting remarkable universality in photoreduction reactions (**Figures 3b-h**). **Figure S9b** shows the photocatalytic activity of C@P/Au-0.25 for 4-NA reduction under different monochromatic light irradiations, exhibiting the optimal performance at an incident wavelength of 500 nm. Combined with the DRS results, this wavelength-dependent activity indicates that the bandgap photoexcitation of the CdS substrate plays a dominant role in governing the photoactivity of the C@P/Au-0.25 heterostructure. In addition to photoactivity, stability is another critical indicator for evaluating the potential practical performance of photocatalysts. Cyclic experiments demonstrate that after 5 consecutive cycles, the photocatalytic activity of C@P/Au-0.25 shows a slight decrease (**Figure S9c**), which may be attributed to mass loss of the catalyst during recovery or minor photocorrosion. Furthermore, the cycled C@P/Au-0.25 were characterized by FTIR (**Figure S10a**), XRD (**Figure S10b**), XPS (**Figure S11**), SEM (**Figure S12a**), and elemental mapping (**Figures S12b-h**). The results indicated that there are no significant changes in the structure and elemental composition of C@P/Au-0.25 heterostructure after cyclic reactions. In summary, these results confirm that C@P/Au-0.25 possesses favorable structural and photochemical stability.

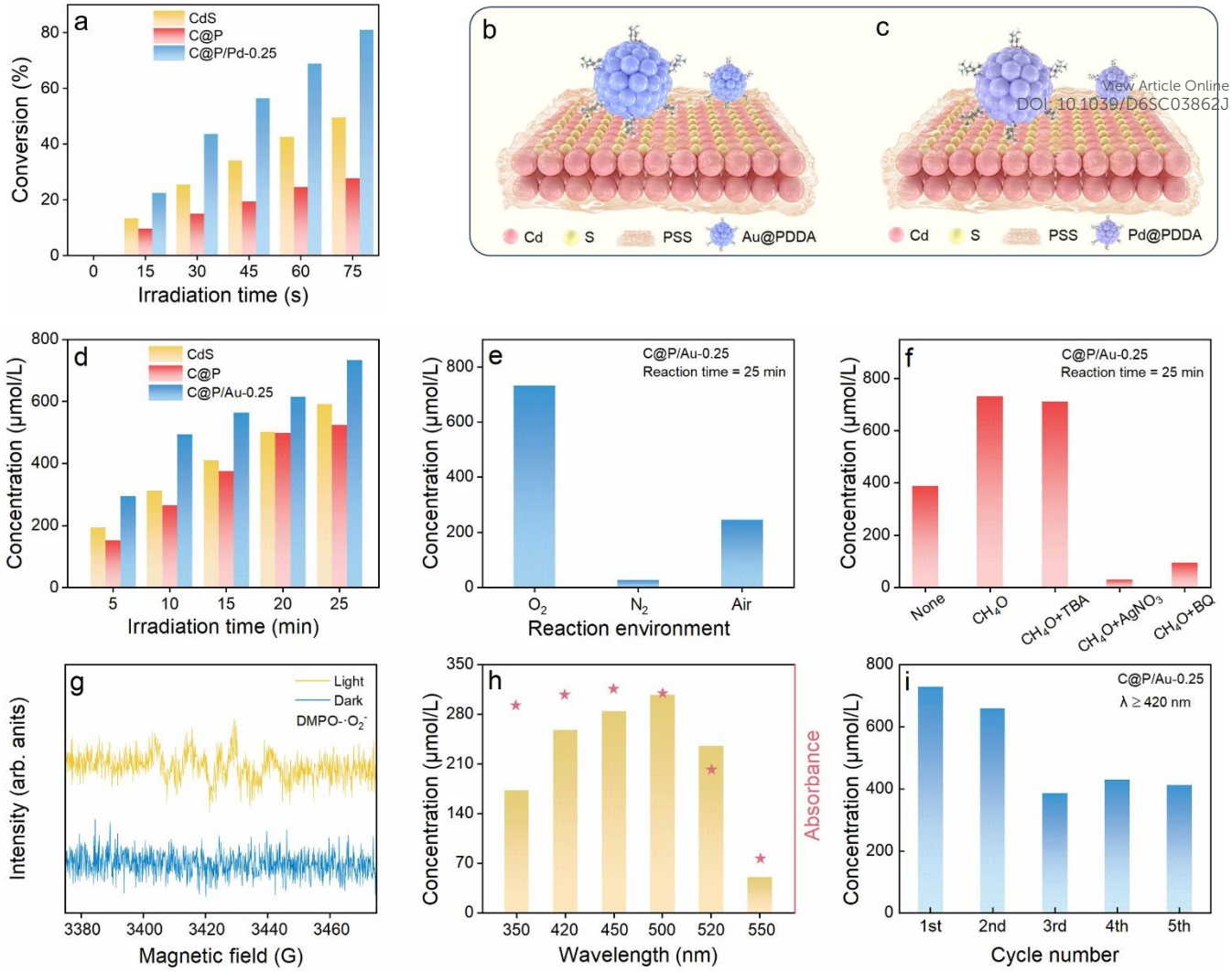

Figure 4. (a) Photocatalytic performances of CdS, C@P and C@P/Pd-0.25 toward selective reduction of 4-NA under visible light irradiation (λ > 420 nm). (b, c) Schematic diagram of the C@P/M (M = Au, Pd) heterostructure model. (d) Comparison of photocatalytic H_2O_2 production performances among CdS, C@P and C@P/Au-0.25 under visible light irradiation (λ > 420 nm) in water with the addition of CH_3OH. (e) Photocatalytic H_2O_2 generation performances of C@P/Au-0.25 in different gas environment. (f) Photocatalytic H_2O_2 production performances of C@P@Au-0.25 upon the addition of different sacrificial agents. (g) EPR spectra of $\cdot O_2^-$ generated over C@P/Au-0.25 under light and dark conditions. (h) Photocatalytic performances of C@P/Au-0.25 under different monochromatic light irradiation. (i) Cyclic reactions of C@P/Au-0.25 for photocatalytic H_2O_2 generation.

To verify the universality of the quantum tunneling mechanism in overcoming interfacial transport resistance, we further constructed different heterostructures and expanded the reaction systems. In addition to Au@PDDA NCs, we also prepared Pd@PDDA NCs (**Figure S13**) and anchored it onto the C@P surface via a similar self-assembly strategy to obtain the C@P/Pd-0.25 heterostructure (**Figure S14**). Experimental results (**Figure 4a**) show that compared with pristine CdS and C@P, C@P/Pd-0.25 also exhibits significantly

enhanced activity in the photocatalytic reduction of aromatic nitro compounds, compellingly confirming the good universality of the M@PDDA (M = Au, Pd)-mediated C@P/M charge transport model (**Figure 4b & c** presents the corresponding schematic illustration).

Furthermore, to deeply reveal the robust capability of this model (C@P/M) in accelerating directional electron migration, we expanded its application scope to the important reaction of photocatalytic H_2O_2 generation and investigated the performance of C@P/Au-0.25 for photocatalytic H_2O_2 production in a water/methanol mixed system. Generally, the pathways for photocatalytic H_2O_2 production include water oxidation reaction and oxygen reduction reaction (ORR).[32, 33] In a methanol system, as demonstrated in our work, holes are effectively scavenged, leaving only electrons to participate in the reaction. Consequently, the generation of H_2O_2 in our current work follows the ORR pathway. As shown in **Figure 4d**, C@P exhibits the lowest photocatalytic activity, whereas C@P/Au-0.25 maintains a significant activity enhancement, achieving a H_2O_2 yield of 733.08 $\mu mol \cdot L^{-1}$ (2511.4 $\mu mol \cdot g^{-1} \cdot h^{-1}$) within 25 minutes. This trend was fully consistent with the results of the photocatalytic performance on reduction of aromatic nitro compounds. Evidently, in the C@P/Au-0.25 heterostructure, it was once again verified that Au@PDDA NCs play a crucial role in attracting electrons and accelerating interfacial electron transport, boosting the charge separation over CdS substrate. To investigate the specific generation mechanism of H_2O_2, atmosphere-regulated experiments and active species trapping tests were performed. **Figure 4e** illustrates the amount of H_2O_2 produced under different atmospheres. The H_2O_2 yield of C@P/Au-0.25 in air atmosphere decreases significantly compared with that in O_2 atmosphere. Moreover, in a N_2 atmosphere where O_2 was completely excluded, photocatalytic activity of the C@P/Au-0.25 heterostructure was almost negligible. This result indicates that O_2 is indispensable in the process of photocatalytic H_2O_2 generation, and its supply directly determines the efficiency of H_2O_2 production. In active species trapping tests, methanol (CH_3OH), tert-butanol (TBA), silver nitrate ($AgNO_3$), and benzoquinone (BQ) served as scavengers for holes (h^+), hydroxyl radicals ($\cdot OH$), electrons (e^-), and

superoxide radicals ($\cdot O_2^-$), respectively, were added into the reaction systems, and then the corresponding photoactivities were evaluated. As shown in **Figure 4f**, compared with the blank photocatalytic system, the H_2O_2 yield produced in the methanol-containing reaction system increases significantly over the same duration, a phenomenon ascribed to the hole trapping boosting the utilization efficiency of electrons. Noteworthily, introduction of $AgNO_3$ induces a substantial reduction in H_2O_2 production, confirming that electrons serve as the core component in the ORR toward H_2O_2 production. Similarly, addition of BQ results in a substantial decrease in H_2O_2 production, a trend that points to $\cdot O_2^-$ radicals being an indispensable active species during the ORR process. In contrast, when TBA was added into the reaction system, the H_2O_2 yield remains virtually unchanged, suggesting that ·OH radicals do not play the predominant role in this reaction.

To further elucidate the generation of ·OH and $\cdot O_2^-$ radicals during the photocatalytic H_2O_2 generation reaction, electron paramagnetic resonance (EPR) spectroscopy of C@P/Au-0.25 heterostructure was utilized. As depicted in **Figure S15**, weak ·OH signals were detected under either dark or illuminated conditions, confirming the minute generation of ·OH radicals during the photocatalytic H_2O_2 generation reaction, which is consistent with the experimental results using TBA as a radical scavenger. Notably, six sets of characteristic DMPO-$\cdot O_2^-$ adduct signals were observed upon light irradiation (**Figure 4g**), implying that $\cdot O_2^-$ is the key active species driving H_2O_2 generation. Based on the comprehensive analysis of the above experimental results, it is concluded that C@P/Au-0.25 catalyzes the generation of H_2O_2 through an indirect two-electron ORR pathway (**Equations 6 & 7**). Consistent with the results of photocatalytic performance on selective reduction of aromatic nitro compounds, C@P/Au-0.25 exhibits the optimal photocatalytic H_2O_2 generation activity at an incident wavelength of 500 nm (**Figure 4h**). Similarly, reusability of the samples toward H_2O_2 generation was also evaluated via cyclic experiments. As displayed in **Figure 4i**, the photocatalytic activity of C@P/Au-0.25 exhibited slight degradation after cycling. To investigate the intrinsic mechanism underlying the stability degradation of the C@P/Au-0.25 photocatalyst, systematic characterization was performed on the sample after

cycling tests. The FTIR spectroscopy (**Figure S16a**), XRD (**Figure S16b**), XPS (**Figure S17**) results demonstrate that the chemical composition and crystal structure of the sample remained consistent with the pristine sample after cycling, without significant changes. However, SEM observation (**Figure S18**) reveals that nano-leaf damage occurred during the reaction process, which constitutes the primary cause of its photocatalytic activity decay. Moreover, benefiting from the efficient charge penetration and separation advantages brought by the quantum tunneling effect at the interface, the C@P/Au composite catalyst constructed in our work exhibits remarkable photocatalytic activity, with performance significantly surpassing that of other CdS-based photocatalysts previously reported (**Tables S4** and **S5**).

$$O_2 + e^- \longrightarrow \cdot O_2^- \quad (E° = -0.33\ V\ vs.\ NHE) \qquad \textbf{(Equation 6)}$$

$$\cdot O_2^- + 2H + e^- \longrightarrow H_2O_2 \quad (E° = +1.44\ V\ vs.\ NHE) \qquad \textbf{(Equation 7)}$$

3.2 PEC and spectroscopic analysis

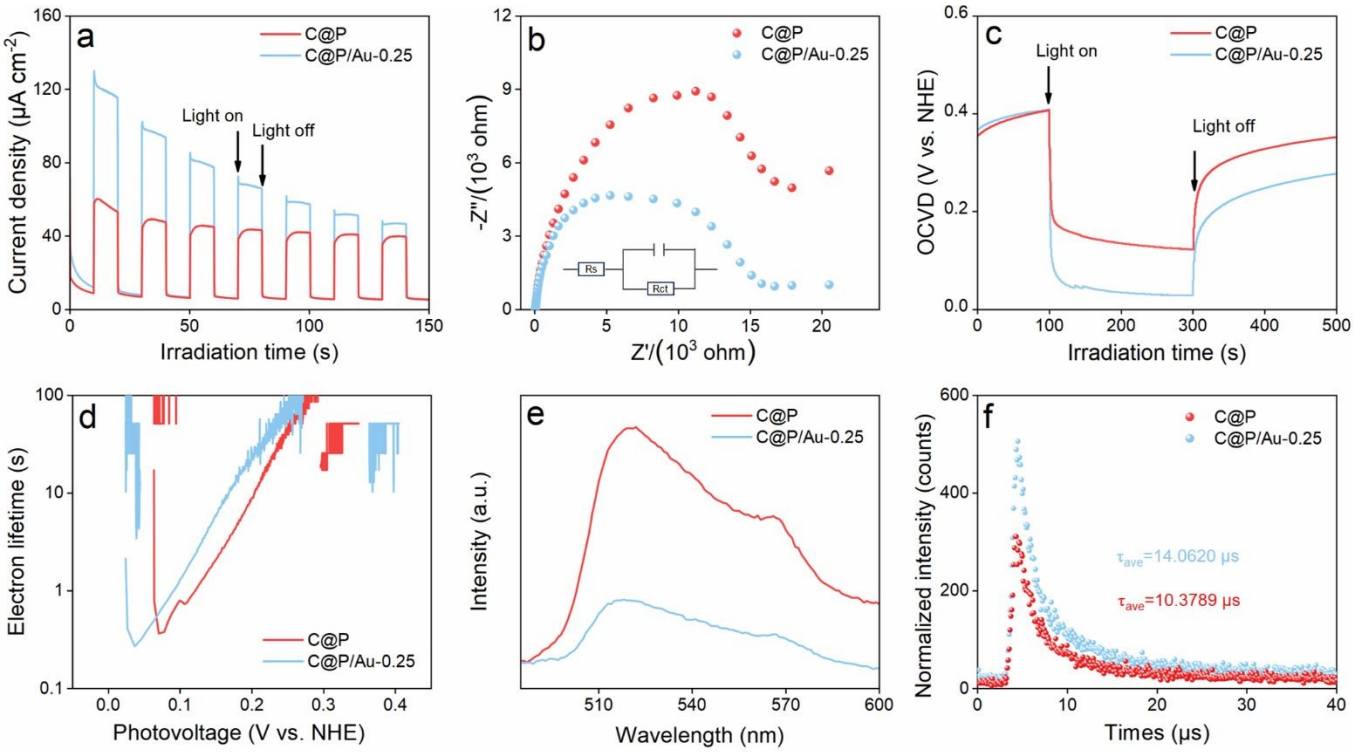

Figure 5. (a) Photocurrent and (b) EIS Nyquist plots of C@P and C@P/Au-0.25 under visible light ($\lambda > 420$ nm) irradiation in an aqueous Na_2SO_4 solution (0.5 M and pH = 6.69), (c) open-circuit potential decay, (d) electron lifetime, (e) PL spectra, and (f) time-resolved transient PL decay.

Photoelectrochemical (PEC) measurements were performed to gain insights into the carrier separation and directional migration behavior of the samples.[34, 35] As displayed in **Figure 5a**, under intermittent visible light irradiation ($\lambda > 420$ nm), C@P/Au-0.25 displays higher photocurrent density than C@P. This finding confirms that, facilitated by the quantum tunneling effect induced by Au@PDDA NCs, photogenerated electrons are able to overcome the insulating restriction of the PSS layer and rapidly transfer from the CdS substrate to Au active centers, thereby enhancing interfacial charge separation efficiency. Consistently, electrochemical impedance spectroscopy (EIS) (**Figure 5b**) combined with fitting results (**Table S6**) collectively verify that introduction of Au@PDDA NCs reduces the interfacial charge transfer resistance (R_{ct}) of C@P/Au-0.25 and thus effectively enhances the charge separation.[36] The open-circuit voltage decay (OCVD) curves were further utilized to analyze charge recombination kinetics. As shown in **Figures 5c & d**, compared with C@P, C@P/Au-0.25 exhibited a higher photovoltage and longer electron lifetime, reaffirming that C@P/Au-0.25 possesses the more enhanced charge separation efficiency. Photoluminescence (PL) and time-resolved photoluminescence (TRPL) tests were utilized to unravel the charge transport dynamics of the catalyst. Typically, PL emission peaks result from the radiative recombination of charge carriers in materials.[37] As shown in **Figure 5e**, PL quenching magnitude of C@P/Au-0.25 is substantially larger than that of C@P with the lower PL emission intensity, strongly indicating that charge recombination of C@P/Au-0.25 is more effectively suppressed. Additionally, the average lifetime of C@P/Au-0.25 (14.0620 μs) is longer than that of C@P (10.3789 μs) (**Figure 5f**). The prolonged carrier lifetime confirms that a substantial proportion of photogenerated electrons do not undergo internal recombination, but rather migrate to Au@PDDA NCs surface active sites via the tunneling mechanism and participate in catalytic reactions.[38] Comprehensive analysis of PEC measurements and PL results reveals that the loading of Au@PDDA NCs significantly reduces the interfacial charge transfer resistance of C@P/Au-0.25, thereby constructing efficient charge separation and transport pathways. This further confirms that Au@PDDA NCs can function as an "electron

pump" to break the transport limitation of the PSS layer, inducing directional migration of photogenerated electrons, which is fully consistent with photocatalytic performances.

View Article Online
DOI: 10.1039/D6SC03862J

3.4 Photocatalytic mechanism

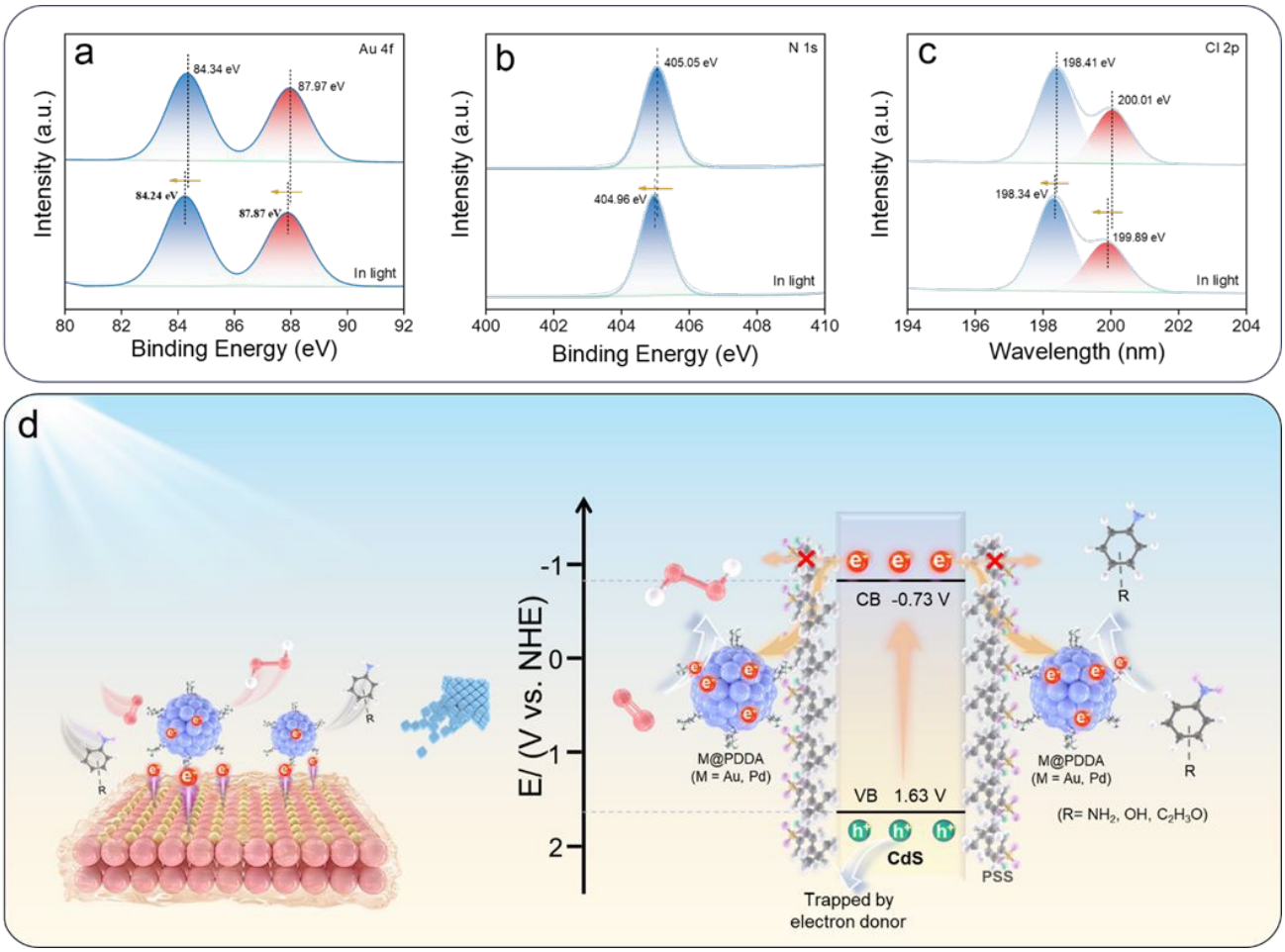

Figure 6. In-situ irradiated high-resolution (a) Au 4f, (b) N 1s and (c) Cl 2p spectra of C@P/Au-0.25. (d) Schematic illustration of the photocatalytic mechanism of the C@P/M-0.25 (M=Au, Pd) heterostructure.

In-situ XPS technology has been recognized as an effective tool to analyze the surface charge transfer mechanisms of photocatalysts. Under photoexcitation, the shift in elemental binding energy can directly reflect the evolution of its local electron density, where an increase in electron density causes the binding energy to shift toward lower energy, and vice versa.[39] Therefore, the shift in binding energy can be used to characterize the migration direction of charge carriers in photocatalysts.[37] As shown in **Figures 6a-c**, compared with the dark conditions, the Au 4f, N 1s, and Cl 2p elements in C@P/Au-0.25 all shift toward lower binding energies under visible light irradiation. This indicates that under visible light illumination, photoelectrons were

transferred from the CdS substrate through the PSS layer to the Au@PDDA NCs, confirming the strong electron-withdrawing property of the Au@PDDA NCs. Evidently, there exists a charge transport chain in the self-assembled C@P/Au-0.25 photosystem that can enhance charge separation efficiency.

Based on the above analysis, we proposed a plausible photocatalytic mechanism for the C@P/Au-0.25 heterostructure (**Figure 7d**). According to the M-S results, flat band potential (E_{fb}) of CdS is -0.63 V vs. NHE (**Figure S19c**). Given that the conduction band (CB) potential (E_{CB}) of n-type semiconductor is 0.1 V more negative than E_{fb}, E_{CB} of CdS is determined to be -0.73 V vs. NHE. Furthermore, DRS result reveals that E_g of CdS is 2.36 eV (**Figure S19a & b**), from which the valence band (VB) potential (E_{VB}) of CdS was calculated to be 1.63 V vs. NHE. This appropriate band structure provided a thermodynamic basis for the photocatalytic reduction of aromatic nitro compounds and the generation of H_2O_2 (**Figure S19d**). When the CdS substrate was coated by an ultrathin PSS layer, the PSS layer inhibits the migration of photogenerated charge carriers to the CdS surface owing to its generic insulating property. Notably, M@PDDA NCs (M = Au, Pd) deposited on the outermost layer of C@P unexpectedly act as high-performance electron-trapping "pump" with excellent electron extraction capability, effectively triggering the tunneling mechanism that penetrates the PSS interlayer and thereby achieving rapid extraction of photogenerated electrons from the CdS surface. This unique interfacial design successfully establishes efficient charge transport channels between CdS and M@PDDA NCs (M = Au, Pd). The detailed charge transport mechanism can be described as follows. Under visible light excitation, CdS is photoexcited to produce electron-hole pairs. Leveraging the powerful electron capture capability of Au@PDDA NCs, electrons on the CB of CdS can through the ultrathin PSS insulating layer via quantum tunneling, thereby driving rapid directional migration of electrons toward the terminal Au@PDDA NCs. In the C@P/Au-0.25 heterostructure, the electrons accumulating on the surface of Au@PDDA NCs efficiently drive the diverse photocatalytic reactions, mainly including two main types. The first reaction was the selective reduction of aromatic nitro compounds, where photogenerated electrons and

protons form azo intermediates through multi-step synergistic effects (**Figure S20**), ultimately converting aromatic nitro compounds into amino derivatives.[40] In this reaction, electrons serve as the sole active species with holes completely quenched by electron donor. The second was H_2O_2 synthesis, which proceeds through the indirect two-electron oxygen reduction pathway, where photogenerated electrons first reduce O_2 to $\cdot O_2^-$, and then, with the assistance of protons, further react with the generated $\cdot O_2^-$ to convert it into H_2O_2.

4. Conclusions

In summary, utilizing non-conjugated insulating polymers as the interlayer, well-defined C@P/M heterostructures were successfully fabricated via a green and easily accessible electrostatic self-assembly strategy under ambient conditions. The terminal M@PDDA NCs, endowed with elegant electron-trapping capability, construct a highly efficient vectorial electron transport pathway within the C@P/M heterostructure with the help of unexpected electron tunneling effect triggered by insulating PSS interlayer, resulting in considerably enhanced charge separation. Ultimately, C@P/M exhibits excellent photoactivity in photocatalytic reduction of aromatic nitro compounds to amino derivatives and photocatalytic synthesis of H_2O_2. By synergistically regulating charge flow through the combination of insulating polymers and metal NCs, this work provides a facile and novel technical avenue for advancing the efficient conversion of solar energy.

Author contributions

Peng Su performed the experiments, analyzed all data, and draft the manuscript. Si-Han Lin help to check the manuscript. Fang-Xing Xiao guided this work and corrected the manuscript. All the authors contributed to a critical discussion on the data and manuscript.

Competing interests

The authors declare no competing interests.

Data availability

View Article Online
DOI: 10.1039/D6SC03862J

The data supporting this article have been included as part of the supplementary information (SI).

Acknowledgements

The support provided by the Program for Minjiang scholar professorship is gratefully acknowledged. This work was financially supported by the National Natural Science Foundation of China (No. 21703038 and 22072025) and Natural Science Foundation of Fujian province (2024J01263). Financial support from the State Key Laboratory of Structural Chemistry, Fujian Institute of Research on the Structure of Matter, and Chinese Academy of Sciences is acknowledged (No. 20240018).

References

1. Z. Y. Teng, H. B. Yang, Q. T. Zhang, W. N. Cai, Y. R. Lu, K. Kato, Z. Z. Zhang, J. Ding, H. Sun, S. X. Liu, C. Y. Wang, P. Chen, A. Yamakata, T. S. Chan, C. L. Su, T. Ohno and B. Liu, Atomically dispersed low-valent Au boosts photocatalytic hydroxyl radical production, *Nat. Chem*. 2024, **16**, 1250-1260.
2. Z. Y. Teng, Z. Z. Zhang, Y. Tu, Q. T. Zhang, N. Jian, L. J. Yang, J. D. Xiao, J. Ding, L. Z. Huang, O. Teruhsia, C. Y. Wang, D. S. Zhang, H. Yu, J. M. Lu, C. L. Su and B. Liu, Asymmetric photooxidation of glycerol to hydroxypyruvic acid over Rb–Ir catalytic pairs on poly(heptazine imides), *Nat. Nanotechnol.*, 2025, **20**, 815-824.
3. X. Yan, J. H. Dong, J. Y. Zheng, Y. Wu and F. X. Xiao, Customizing precise, tunable, and universal cascade charge transfer chains towards versatile photoredox catalysis, *Chem. Sci.,* 2024, **15**, 2898-2913.
4. P. Su, X. Yan and F. X. Xiao, Customizing dumbbell-shaped heterostructured artificial photosystems steering versatile photoredox catalysis, *Chem. Sci.,* 2024, **15**, 14778-14790.
5. J. H. Han, M. Kwak, Y. Kim and J. Cheon, Recent Advances in the Solution-Based Preparation of Two-Dimensional Layered Transition Metal Chalcogenide Nanostructures, *Chem. Rev.*, 2018, **118**, 6151-6188.
6. P. Su, Y. H. Chen, F. X. Xiao and Y. J. Xu, Dual-Oxidative Co-Catalyst Synergy Regulating Charge Transport Cascade for Enhanced CO_2 Photocatalysis, *Small*, 2026, **22**, e11429.
7. X. Z. Ge, K. Wang, Q. L. Mo, Y. Xiao, J. L. Li, G. Wu, S. R. Xu and F. X. Xiao, Non-conjugated polymer ligand: stimulating charge transfer towards photocatalytic selective organic transformation, *Catal. Sci. Technol.,* 2023, **13**, 479-489.

8. Y. Jiang, H. B. Sun, J. Y. Guo, Y. S. Liang, P. F. Qin, Y. Yang, L. Luo, L. J. Leng, X. M. Gong and Z. B. Wu, Vacancy Engineering in 2D Transition Metal Chalcogenide Photocatalyst: Structure Modulation, Function and Synergy Application, *Small*, 2024, **20**, 2310396.
9. R. Shi, Y. H. Cao, Y. J. Bao, Y. F. Zhao, G. I. N. Waterhouse, Z. Y. Fang, L. Z. Wu, C. H. Tung, Y. D. Yin and T. R. Zhang, Self-Assembled Au/CdSe Nanocrystal Clusters for Plasmon-Mediated Photocatalytic Hydrogen Evolution, *Adv. Mater.*, 2017, **29**, 1700803.
10. H. Wang, X. Y. Zhang, W. Zhang, M. Zhou and H. L. Jiang, Heteroatom-Doped Ag_{25} Nanoclusters Encapsulated in Metal–Organic Frameworks for Photocatalytic Hydrogen Production, *Angew. Chem. Int. Ed.*, 2024, **63**, e202401443.
11. T. Li, M. H. Huang, Y. B. Li, X. C. Dai, Y. H. He, G. C Xiao and F. X. Xiao, General self-assembly of metal/metal chalcogenide heterostructures initiated by a surface linker: modulating tunable charge flow toward versatile photoredox catalysis, *J. Mater. Chem. A*, 2019, **7**, 21182-21194.
12. C. Du, B. Yan, Z. Y. Lin and G. W. Yang, Enhanced carrier separation and increased electron density in 2D heavily N-doped $ZnIn_2S_4$ for photocatalytic hydrogen production, *J. Mater. Chem. A*, 2020, **8**, 207-217.
13. B. Tang, S. C. Zhu, H. Liang, S. Li, B. J. Liu and F. X. Xiao, Tuning atomically precise metal nanocluster mediated photoelectrocatalysis via a non-conjugated polymer, *J. Mater. Chem. A*, 2022, **10**, 4032-4042.
14. B. Weng, K. Q. Lu, Z. C. Tang, H. M. Chen and Y. J. Xu, Stabilizing ultrasmall Au clusters for enhanced photoredox catalysis, *Nat. Commun.*, 2018, **9**, 1543.
15. Q. C. Xu, J. X. Zeng, H. Q. Wang, X. Y. Li, J. Xu, J. Y. Wu, G. C. Xiao, F. X. Xiao and X. Y. Liu, Ligand-triggered electrostatic self-assembly of CdS nanosheet/Au nanocrystal nanocomposites for versatile photocatalytic redox applications, *Nanoscale*, 2016, **8**, 19161-19173.
16. S. C. Han, L. F. Hu, N. Gao, A. A. Al-Ghamdi and X. S. Fang, Efficient Self-Assembly Synthesis of Uniform CdS Spherical Nanoparticles-Au Nanoparticles Hybrids with Enhanced Photoactivity, *Adv. Funct. Mater.*, 2014, **24**, 3725-3733.
17. Z. Q. Wei, S. Hou, X. Lin, S. Xu, X. C. Dai, Y. H. Li, J. Y. Li, F. X. Xiao and Y. J. Xu, Unexpected Boosted Solar Water Oxidation by Nonconjugated Polymer-Mediated Tandem Charge Transfer, *J. Am. Chem. Soc.*, 2020, **142**, 21899-21912.
18. X. Yan, K. Wang and F. X. Xiao, Electron Tunneling Fosters Solar-to-Hydrogen Energy Conversion, *Inorg. Chem.*, 2023, **62**, 17454-17463.

19. P. Su, B. Tang and F. X. Xiao, Layer-By-Layer Assembly of Atomically Precise Alloy Nanoclusters Photosystems for Solar Water Oxidation, *Small*, 2024, **20**, 2307619.

View Article Online
DOI: 10.1039/D6SC03862J

20. Q. L. Mo, J. L. Li, S. R. Xu, K. Wang, X. Z. Ge, Y. Xiao, G. Wu and F. X. Xiao, Unexpected Insulating Polymer Maneuvered Solar CO_2-to-Syngas Conversion, *Adv. Funct. Mater.*, 2023, **33**, 2210332.

21. K. Wang, M. Wang, H. Y. Xie, S. L. Li, X. Kong and Z. L. Jin, Rational construction of graphdiyne (g-C_nH_{2n-2}) coupling with Co-Co PBA S-scheme heterojunctions for efficient photocatalytic hydrogen production, *Sep. Purif. Technol.*, 2023, **322**, 124286.

22. H. I. Kim, Y. Choi, S. Hu, W. Y. Choi and J. H. Kim, Photocatalytic hydrogen peroxide production by anthraquinone-augmented polymeric carbon nitride, *Appl. Catal. B Environ. Energy*, 2018, **229**, 121-129.

23. Q. Y. Wu, J. J. Cao, X. Wang, Y. Liu, Y. J. Zhao, H. Wang, Y. Liu, H. Huang, F. Liao, M. W. Shao and Z. H. Kang, A metal-free photocatalyst for highly efficient hydrogen peroxide photoproduction in real seawater, *Nat. Commun.*, 2021, **12**, 483.

24. Q. Chen, Y. H. Chen, J. R. Zhu, Z. Y. Li and F. X. Xiao, Customizing Synchronous Charge Tunneling Photosystems Toward Solar CO_2 Conversion, *Adv. Funct. Mater.*, 2025, **35**, 2417139.

25. C. X. Li, L. J. Han, R. J. Liu, H. H. Li, S. J. Zhang and G. J. Zhang, Controlled synthesis of CdS micro/nano leaves with (0001) facets exposed: enhanced photocatalytic activity toward hydrogen evolution, *J. Mater. Chem.*, 2012, **22**, 23815-23820.

26. J. V. Antony, P. Kurian, N. P. N. Vadakkedathu and G. E. Kochimoolayil, In Situ Synthesis of CdS Quantum Dot–Partially Sulfonated Polystyrene Composite: Characterization and Optical Properties, *Ind. Eng. Chem. Res.*, 2014, **53**, 2261-2269.

27. R. S. Jing, J. S. Yang, S. T. Li, S. F. Zhao, P. F. Wang, Y. Y. Liu, A. J. Liu, Z. L. Meng, H. W. Huang, Z. L. Zhang and Q. Zhang, Construction of PDDA functionalized black phosphorus nanosheets/BiOI Z-scheme photocatalyst with enhanced visible light photocatalytic activity, *J. Colloid Interface Sci.*, 2020, **576**, 34-46.

28. F.-X. Xiao, Z. P. Zeng and B. Liu, Correction to "Bridging the Gap: Electron Relay and Plasmonic Sensitization of Metal Nanocrystals for Metal Clusters", *J. Am. Chem. Soc.*, 2015, **137**, 13990-13990.

29. F.-X. Xiao, Layer-by-Layer Self-Assembly Construction of Highly Ordered Metal-TiO_2 Nanotube Arrays Heterostructures (M/TNTs, M = Au, Ag, Pt) with Tunable Catalytic Activities, *J. Phys. Chem. C*, 2012, **116**, 16487-16498.

30. G. Wang, R. Huang, J. W. Zhang, J. J. Mao, D. S. Wang and Y. D. Li, Synergistic Modulation of the Separation of Photo-Generated Carriers via Engineering of Dual Atomic Sites for Promoting Photocatalytic Performance, *Adv. Mater.*, 2021, **33**, 2105904.

31. B. Lin, H. Li, H. An, W. B. Hao, J. J. Wei, Y. Z. Dai, C. S. Ma and G. D. Yang, Preparation of 2D/2D g-C_3N_4 nanosheet@$ZnIn_2S_4$ nanoleaf heterojunctions with well-designed high-speed charge transfer nanochannels towards high-efficiency photocatalytic hydrogen evolution, *Appl. Catal. B Environ. Energy*, 2018, **220**, 542-552.

32. J. D. Yang, X. K. Zeng, M. Tebyetekerwa, Z. Y. Wang, C. B. Bie, X. Sun, I. Marriam and X. W. Zhang, Engineering 2D Photocatalysts for Solar Hydrogen Peroxide Production, *Adv. Energy Mater.*, 2024, **14**, 2400740.

33. Z. Y. Teng, Q. Zhang, H. B. Yang, K. Kato, W. J. Yang, Y. R. Lu, S. X. Liu, C. Y. Wang, A. Yamakata, C. L. Su and B. Liu, T. Ohno, Atomically dispersed antimony on carbon nitride for the artificial photosynthesis of hydrogen peroxide, *Nat. Catal.*, 2021, **4**, 374-384.

34. P. Su, J. L. Liu and F. X. Xiao, Optimization of electron transfer pathways in atomically precise metal nanoclusters: catalyzing a leap in solar water oxidation, *Chem. Sci.,* 2026, **17**, 3300-3312.

35. B. Wang, J. Z. Zhao, H. L. Chen, Y. X. Weng, H. Tang, Z. R. Chen, W. S. Zhu, Y. B. She, J. X. Xia and H. M. Li, Unique Z-scheme carbonized polymer dots/$Bi_4O_5Br_2$ hybrids for efficiently boosting photocatalytic CO_2 reduction, *Appl. Catal. B Environ. Energy*, 2021, **293**, 120182.

36. A. P. Singh, N. Kodan, B. R. Mehta, A. Held, L. Mayrhofer and M. Moseler, Band Edge Engineering in $BiVO_4/TiO_2$ Heterostructure: Enhanced Photoelectrochemical Performance through Improved Charge Transfer, *ACS Catal.*, **2016, 6**, 5311-5318.

37. L. B. Wang, B. Cheng, L. Y. Zhang and J. G. Yu, In situ Irradiated XPS Investigation on S-Scheme TiO_2@$ZnIn_2S_4$ Photocatalyst for Efficient Photocatalytic CO_2 Reduction, *Small*, 2021, **17**, 2103447.

38. S. Nayak, L. Mohapatra and K. Parida, Visible light-driven novel g-C_3N_4/NiFe-LDH composite photocatalyst with enhanced photocatalytic activity towards water oxidation and reduction reaction, *J. Mater. Chem. A*, 2015, **3**, 18622-18635.

39. L. B. Wang, B. C. Zhu, B. Cheng, J. J. Zhang, L. Y. Zhang and J. G. Yu, In-situ preparation of TiO_2/N-doped graphene hollow sphere photocatalyst with enhanced photocatalytic CO_2 reduction performance, *Chin. J. Catal.*, 2021, **42**, 1648-1658.

40. H. Liang, B. J. Liu, B. Tang, S. C. Zhu, S. Li, X. Z. Ge, J. L. Li, J. R. Zhu and F. X. Xiao, Atomically Precise Metal Nanocluster-Mediated Photocatalysis, *ACS Catal.*, 2022, **12**, 4216-4226.

View Article Online
DOI: 10.1039/D6SC03862J

Data availability statements

The data supporting this article have been included as part of the Supplementary Information.